metals

MDPI

Article

Lattice Boltzmann Method Modeling of the Evolution of Coherent Vortices and Periodic Flow in a Continuous Casting Mold

Peng Zhao [1] and Rongxun Piao [2,*]

[1] School of Materials Science and Engineering, Shandong Jianzhu University, Jinan 250101, China; zhaopeng3@hotmail.com
[2] Department of Mechanical Engineering, Anhui University of Science and Technology, Huainan 232001, China;
* Correspondence: yhpark617@163.com

Abstract: Transient phenomena and vortex structures throughout the mold are simulated using a lattice Boltzmann method (LBM) coupled with large eddy simulation (LES) using a free surface model under steady operating conditions. The accuracy of the LBM-LES model has been verified by comparing the simulated velocities with published experimental values. The current work focuses on the evolution of the vortex structure in internal flow inside the submerged entry nozzle (SEN) jet flow and the turbulent flow near the wall of the mold. The results show various types of vortex structures with different directions are presented during the jet impingement, including the "ring, rib, and horseshoe"-like shaped vortices in the simulation, resulting in complex turbulent flow near the wall of the mold. Vortices structures are then identified and compared by different vorticial criteria, including vortex methods (ω), Q method, $\lambda 2$ method (Lambda-2), Δ method (Delta), and Ω method (Omega). The formation, development, and dissipation of the vortex structures and their effects on turbulence are investigated. The results indicate that the turbulent flow (viscosity) can reflect changes in asymmetric vortices structures and flow patterns (via crossflow), which can reflect the periodical flow in the mold. Flow oscillation frequencies are mainly concentrated in the range of 0.3 Hz in this simulation. The oscillations are not a simple combination of frequency modes of crossflow in the mold. These new studies can elucidate the mechanism of vortex structure distributions in representative flow regions of the continuous casting mold.

Keywords: continuous casting; fluid dynamics; coherent vortices; numerical modeling

check for updates

Citation: Zhao, P.; Piao, R. Lattice Boltzmann Method Modeling of the Evolution of Coherent Vortices and Periodic Flow in a Continuous Casting Mold. *Metals* **2022**, *12*, 572. https://doi.org/10.3390/met12040572

Academic Editor: Alexander McLean

Received: 15 January 2022
Accepted: 23 March 2022
Published: 28 March 2022

1. Introduction

Molten steel emerging from a submerged entry nozzle (SEN) presents transient characteristics and flows into the mold cavity of the continuous caster. Various flow structures significantly affect the quality of the final products. Some reviews of the multiphase phenomena during continuous casting and their modeling have been published in recent years [1–3]. Steelmakers have had to rely on plant trials and physical property measurements on fluxes and steels to understand the mechanisms responsible for operational process problems and product defects. Mathematical modeling has been proven to provide us with insight into these mechanisms, including heat transfer, solidification, multiphase turbulent flow, clogging, electromagnetic effects, complex interfacial behavior, particle entrapment, etc. Some of these phenomena seem simple and may appear easy to control through the main casting parameters; however, when combined, these phenomena exhibit periodic fluctuations, which are both difficult to predict and control, giving rise to the "butterfly effect" as seen in continuous casting over the extended length and time scales.

Further advances will require a better understanding of the fundamental behavior, which is difficult to realize with experiments in this harsh environment. Many mathematical models have investigated how turbulent structures exert a direct effect on solidification [4,5].

Air aspiration through an SEN tube can cause reoxidation and leave nonmetallic inclusions that may adhere to the refractory walls of the SEN, clogging the nozzle. Asymmetric jet flow from a clogged nozzle causes excessive surface velocities and vorticial flow at the top surface in the mold, resulting in slag entrainment within the steel pool. Instability at the interface between the molten steel and surface slag can cause the jet to wobble, leading to slag entrapment within the solidifying shell at the meniscus region. This surface defect formation intensifies upon freezing of the meniscus and the accompanying formation of subsurface hooks. The mushy zone and solid shell formed during solidification of a continuous casting are mostly uneven, and this unevenness of shell growth may lead to surface defects or breakout. Furthermore, particles such as argon gas bubbles, alumina inclusions, and entrained slag droplets can be transported deep into the slab and captured within the steel shell; this is closely related to defect formation in continuous steel casting.

Many numerical studies have covered the instabilities and possible asymmetry of the melt flow in the mold of a continuous slab caster under the influence of a direct current (DC) magnetic field (electromagnetic brakes (EMBrs)), which is the dominant flow-control technique used to counteract the described undesired phenomena arising in continuous casting. Vakhrushev [6] and Kharicha [7] showed how the restructuring of the coherent turbulent structures causes the redistribution of the linear momentum of the melt flow under the applied magnetic field. The generation of reverse meniscus flow can be explained as a magnetohydrodynamic (MHD) effect: (1) the closure of the induced electric current results in an acceleration in regions of weak velocities, which initiates the formation of an opposite vortex close to the main jet; (2) this vortex develops in size at the expense of the main vortex until it reaches the meniscus surface. That can lead to the acceleration of the meniscus and to the formation of the reversal flow zones. Thomas and Cho [8–10] detailed the action types and effects from the EMBr forces on the formation of solidification defects in a continuous casting process.

The instantaneous turbulence and vortex structures play an essential role in many complicated transfer phenomena; this has been studied by macroscopic mathematical models coupled with the LES model, which provides more details of the instantaneous turbulence. Many researchers simulated the transient flow and related phenomena in a continuous caster using the LES model. Real et al. [11] studied the periodic flow behavior in SEN using the LES model. Yuan et al. [12] identified "stair-step" jets using the LES models, showing good agreement between the calculated and measured velocities using the LES and experimental measurements. Liu et al. [13–17] further developed various computational fluid dynamics (CFD) methods coupled with the LES model, an Euler–Euler approach, and a scale-adaptive simulation method to simulate asymmetrical phenomena at both sides of the mold. They have investigated the bubble, the strip feeding, the inhomogeneous vorticity distribution inside the mold using the vorticity w. Previous research [18] further extracted the coherent vortices from the asymmetric flow during the steady-state condition of the continuous casting process using Q criterion that can better acquire structures present at a mesoscale level. Recently, the Lattice Boltzmann Method (LBM) has been widely used, especially for complicated flow systems. This mesoscale approach combines the advantages of the macro continuum model and the micromolecular dynamics method. The LBM model coupled with the LES frame has been successfully applied to the continuous casting process. Pirker et al. [19] predicted horizontally orientated secondary vortices and the gas bubble threads in the deflection zone of SEN through hybrid finite volume and lattice Boltzmann models. The simulation results prove that an LBM-LES mesoscopic model is verifiable and acceptable modeling for predicting transient flows and demonstrating the method potential in terms of complicated flow at very small scales, compared with the Reynolds-averaged Navier–Stokes equations (RANS) that only can obtain time-averaged variables.

It is necessary to determine vortex structures in turbulent flow and obtain asymmetric patterns through various vortices criteria, and these mechanisms need to be further elucidated. The research on the relationship between the vorticial structures in typical flow regions in the continuous casting mold is not comprehensive. The asymmetrical exchange

of the vorticial structures on the turbulent flow and periodic mirror-like images are unclear. Based on the prospective merits of different vorticial criteria, this study focuses on coherent structures in typical flow in the mold using LBM-LES models. The influences of the solidification, mold slag and argon bubbles on the molten steel flow are not considered in the simulation. The LBM-LES model is established to simulate the transient flow of molten steel with a free surface model. The applicability of the model is validated by comparing the simulated results with the velocity profiles measured experimentally. Various vortex structures are identified and compared by different vorticial criteria, including vortex method w, Q method, $\lambda 2$ method (Lambda-2), Δ method (Delta), and Ω method (Omega). Thereafter, the evolution of coherent vortices in typical flow regions inside the mold is investigated, turbulent flow around the vortex structures and the frequency arising from crossflow inside the mold are also studied.

2. Model Formulation

2.1. LBM Model

Lattice Boltzmann Method is given by [20]:

$$f_i(x + c_i, t + \delta t) - f_i(x, t) = \frac{1}{\tau_{\mathrm{LB}}}(f_i(x, t) - f_i^{\mathrm{eq}}(x, t)) + \vec{F}_i \tag{1}$$

where c_i represents the discrete lattice velocities, δ denotes the time step, $f_i(x, t)$ is the discretized distribution functions, τ_{LB} represents the dimensionless relaxation time, $\vec{F}$ is the gravitational force adopted into the LBM model, and $f_i^{\mathrm{eq}}(x, t)$ is Maxwell distribution equilibrium function given by:

$$f_i^{\mathrm{eq}}(x, t) = \rho w_i \left[1 + \frac{c_i \cdot u}{C_s^2} + \frac{(c_i \cdot u)^2}{2C_s^4} - \frac{u^2}{2C_s^2}\right] \tag{2}$$

where C_s is the sound speed.

w_i is weight according to the lattice discretization, and i is a range from 0 to 18, as follows:

$$w_i = \left\{ \begin{array}{cc} \frac{1}{3} & i = 0 \\ \frac{1}{18} & i = 1 - 6 \\ \frac{1}{36} & i = 7 - 8 \end{array} \right\} \tag{3}$$

The model D3Q19 is applied for the LBM model, and the collision operator employs the Bhatnagar–Gross–Krook (BGK) model with a single relaxation time [21].

The macroscopic quantities are calculated by taking the moments of distribution functions:

$$\rho = \sum_i f_i \tag{4}$$

$$\rho u = \sum_i c_i f_i \tag{5}$$

where ρ is the macroscopic density, and u is the macroscopic velocity.

2.2. LES Model

The subgrid-scale stresses τ_{ij} is defined by Smagorinsky subgrid model [22]:

$$\tau_{ij} - \frac{1}{3}\delta_{ij}\tau_{kk} = -2v\overline{S}_{ij} \tag{6}$$

where δ_{ij} is the Kronecker delta function, the isotropic part of the Reynolds stress term τ_{kk} is included in the pressure term, the subscripts i and j represent three Cartesian directions.

$\overline{S}_{ij}$ is expressed as the rate of large-scale strain tensor given by

$$\overline{S}_{ij} = \frac{1}{2}\left(\frac{\partial \overline{u}_i}{\partial x_j} + \frac{\partial \overline{u}_j}{\partial x_i}\right) \tag{7}$$

The viscosity v in the Smagorinsky model is defined as:

$$v = v_0 + v_{\text{eddy}} \tag{8}$$

where v_0 is the kinematic viscosity, and v_{eddy} is eddy viscosity given by:

$$v_{\text{eddy}} = \text{C}\Delta^2\left|\overline{S}\right| \tag{9}$$

where Δ is expressed as the minimum size; C is the Smagorinsky constant, which depends on the size of the grid, and the value ranges between 0.1 and 0.2.

Relaxation time τ_{LB} can be expressed as:

$$\tau_{\text{LB}} = 3\left(v_0 + \text{C}\Delta^2\left|\overline{S}\right|\right) + \frac{1}{2} \tag{10}$$

where $\left|\overline{S}\right|$ is the intensity of the local filtered stress tensor given by:

$$\left|\overline{S}\right| = \frac{\sqrt{v_0^2 + 18\text{C}\Delta^2\sqrt{\overline{\Pi}_{i,j}\overline{\Pi}_{i,j}}} - v_0}{6\text{C}\Delta^2} \tag{11}$$

where $\overline{\Pi}_{i,j} = \sum_{\alpha} c_{\alpha i}c_{\alpha j}\left|\overline{f}_i - \overline{f}_i^{\text{eq}}\right|$ is the local nonequilibrium stress tensor.

2.3. Free Surface Model

The free interface between the two phases is solved using the filled fraction α. When α is 0 or 1, it is expressed as an empty cell or a full cell; when α is close to 1 or 0, it indicates that the lattice changes between the interface, the liquid, and the gas cell. The mass of the liquid phase at the interface is given by [23]:

$$m = \alpha(\Delta x)^3\rho \tag{12}$$

The interface is tracked by calculating the mass change between the adjacent cells. The mass balance between the liquid phase and interface lattice is defined by:

$$\Delta m_i(x,t) = \left\{\begin{array}{ll} 0 & x + c_i \text{ is gas} \\ f_{\tilde{i}}(x + c_i, t) - f_i(x,t) & x + c_i \text{ is liquid} \\ \frac{\alpha(x+c_i,t)+\alpha(x,t)}{2}\left[f_{\tilde{i}}(x + c_i, t) - f_i(x,t)\right] & x + c_i \text{ is interface} \end{array}\right\} \tag{13}$$

The mass exchange is directly calculated by the distribution function. The mass exchange between the two interface lattices should meet the mass conservation as follows:

$$\Delta m_i(x,t) = -\Delta m_{\tilde{i}}(x + c_i) \tag{14}$$

When $m < 0$ or $m > 0$, the interface lattice is respectively transformed into a gas phase or a liquid phase lattice so that a new interface lattice is formed. The equation of the mass change of the interface is defined by:

$$\Delta m(x, t + \Delta t) = \Delta m(x,t) + \sum_{i=0}^{18}\Delta m_i(x, t + \Delta t) \tag{15}$$

3. Establishing and Validating Model

3.1. Calculation

The computation is conducted using the LBM model, which conducted using an in-house code.

The lattice spacing is set to 2 mm, which results in a total of 800,000 elements in the LBM model. The time step for these simulations is 0.02 s. The resolved scale is 0.005 m. The starting time step for these simulations is 0.001 s. The inlet and outlet boundary conditions in the model are based on the bounce-back condition for the nonequilibrium portion of the distribution. The constant velocity inlet boundary condition is based on the casting speed at the inlet of SEN. The pressure outlet condition is applied in these calculations. The Paraview, an open-source software package, is employed to accomplish simulation post-processing for transient flow fields and vortex structures induced by different criteria. Table 1 lists the geometrical SEN and mold cavity, simulation conditions, and operating parameters considered in the simulation.

Table 1. Simulation conditions considered in the model.

Parameter	Value
Mold width (m)	1.2
Mold thickness (m)	0.23
Casting speed (m·min^{-1})	1.4
SEN submergence depth (mm)	100
SEN port angle (deg)	15°
SEN port shape	Rectangle
SEN port height (mm)	45
SEN port width (mm)	35
Molten steel density (kg·m^{-3})	7020
Molten steel viscosity (Pa·s)	0.0056

The basic form of wall modeling for LES simply imposes additional constraints on the eddy viscosity. To reduce overpredicts turbulent viscosity, especially near the wall, the velocity is calculated using the Van Driest [24] damping function into the length scale to reflect the nature of such coherent structures in turbulent flow (Re > 10000) inside the mold, as follows:

$$L = \mathrm{C}\Delta\left[1 - \exp\left(-\frac{-y^+}{A^+}\right)\right] \tag{16}$$

where y^+ denotes the dimensionless distance, Δ is the feature length, $\Delta = V^{1/3}$, and A^+ is a constant.

3.2. Validation

To validate the accuracy of the LBM model, predicted velocity profiles are compared with previous experimental measurements, and the details of geometry and operating conditions are available elsewhere [25]. Figure 1 shows the predicted velocity profiles in the simulation against the time-averaged velocities at different times in the experiment. The measurements are made along two vertical lines in the center plane at a distance of 51 mm and 102 mm from the SEN, respectively. The results show that the velocity profiles changes with the distances from the SEN. Simulated velocities profiles at the distance of 51 mm have higher values compared with those at the distance of 102 mm. As can be seen from the figure, the predicted velocities were in good agreement with measured data. There are some minor differences at a distance of 102 mm from SEN. This might be due to uncertainties in the experimental measurements or the averaged results thereof.

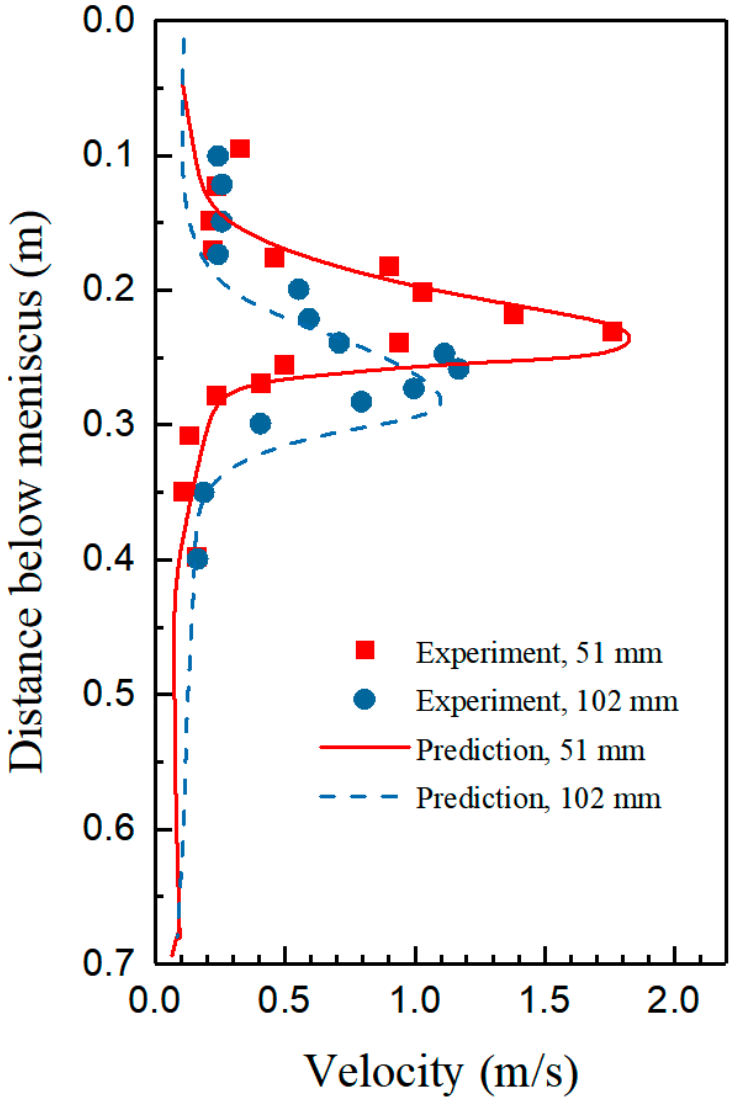

Figure 1. Comparison of predicted velocities in the LBM model and measurements in a water model at a distance of 51 mm and 102 mm from the SEN [25].

4. Results and Discussion

In a previous paper, transient phenomena and vorticial structures throughout the mold are characterized using the LBM-LES model. Differing from that previous work, in the current research, we update the description of the formation, development, and dissipation of the vortex structures and their effects on turbulence in representative flow regions of the continuous casting mold in detail, as described herein.

4.1. Evolution of Coherent Vortices

There are multiphase and complex transport phenomena such as flow, heat transfer, mass transfer, and solidification arising in the mold. These processes with multiphase and multiscale characteristics are interrelated and interact. Figure 2 schematically shows the representative flow regions, including SEN outflow, jet flow, and wall flow in the mold of the continuous caster.

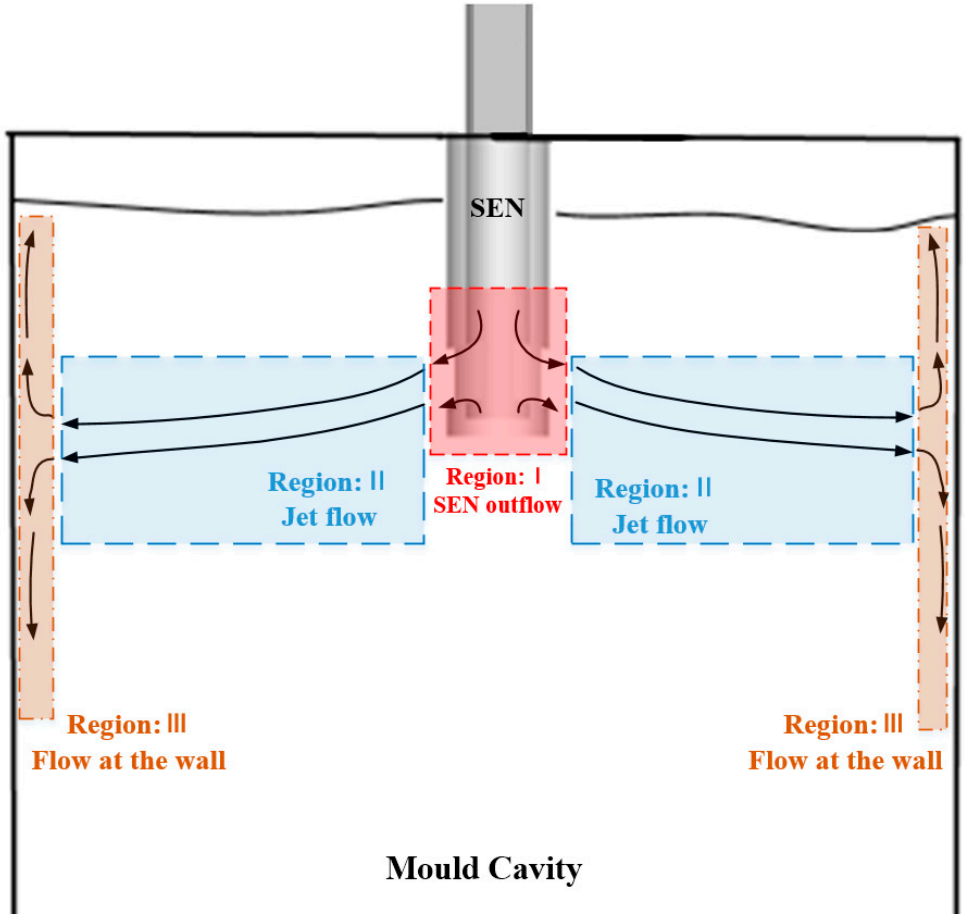

Figure 2. A typical flow region includes SEN outflow, jet flow, surface flow, and wall flow inside the mold.

4.1.1. SEN Outflow

The mold has a submerged bifurcated nozzle with a bottom wall. The molten steel enters the SEN from the submerged upper pipe of the mold. Multi-scaled vortices inevitably exist in the turbulent flow of the mold. Figure 3 shows transient coherent vortices inside the SEN from different views with the Q criterion (Q = 200) given by [26]:

$$Q = -\frac{1}{2}\frac{\partial u_i}{\partial x_j}\frac{\partial u_j}{\partial x_i} = \frac{1}{2}\left(\Omega_{ij}\Omega_{ij} - \Psi_{ij}\Psi_{ij}\right) > 0 \tag{17}$$

where Ω_{ij} and Ψ_{ij} represent the symmetric and antisymmetric components of ∇u, respectively; The vortex structures deduced from the Q criterion are shown in the flow region (at the middle region), mainly distributed in the upper flow separation point (the upper corner) and the bottom structure (concave shape) of the SEN, respectively. The internal structures of the SEN affect the internal flow in this region. The formation of coherent vortices occurs at the upper corner of the SEN, akin to the flow separation seen at the backflow step. Coherent vortices then develop toward the SEN outlet, and those are also concentrated near the concave shape of the SEN bottom. Coherent vortices split into small vortices and interact, resulting in a complex flow regime within the mold, as shown in Figure 2 (Region I).

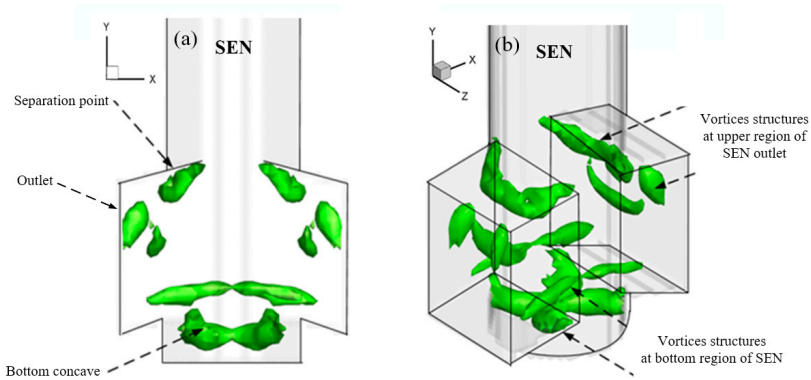

Figure 3. Distribution of the coherent structures inside the SEN from different views: (**a**) at the middle and (**b**) 3D perspective.

4.1.2. Jet Diffusion

The jet from the SEN outlet exhibits a "stair-step" oscillation characteristic and develops along the width until it attacks the wall of the mold. The transient jet produces many large-scale swirling vortices and small-scale vortices in this region. Taking the vortex structure of the jet flow on the left-hand side of the mold as an example, Figure 4 shows the development of the vortex structure in the jet flow region across the width of the mold at different times (Q = 100). The jet flow with specific kinetic energy from SEN forms a rapidly expanding bulge and develops a vortex ring structure during the jet flow diffusion. The vortex ring, accompanied by the braided region, also develops along with separated vortex structures until they reach together the narrow wall of the mold. Furthermore, Figure 5 illustrates the shape of the ring structures and their surrounding tangential vectors: vectors rotate around the vortex ring, which may cause the jet to wobble. Thus, vortex structures with vectors in the jet flow region can reveal the dynamic characteristics of the jet in the mold.

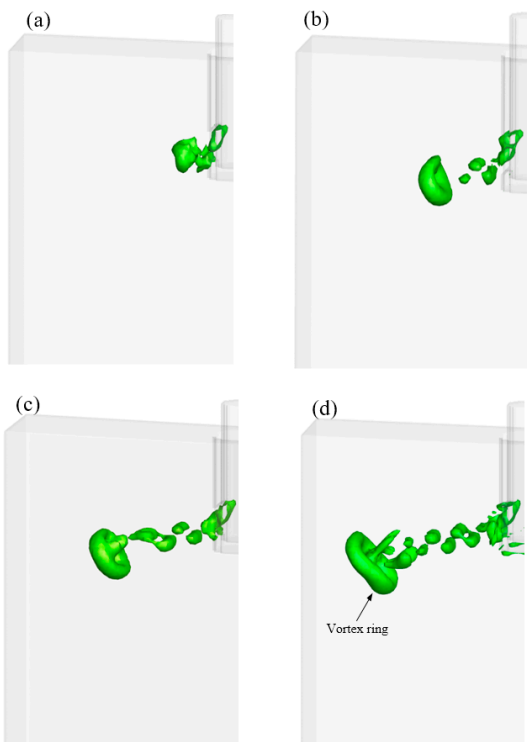

Figure 4. Development of the vortex structure in the jet flow region across the width of the mold at different times of (**a**) 0.2 s, (**b**) 0.3 s, (**c**) 0.4 s, and (**d**) 0.5 s.

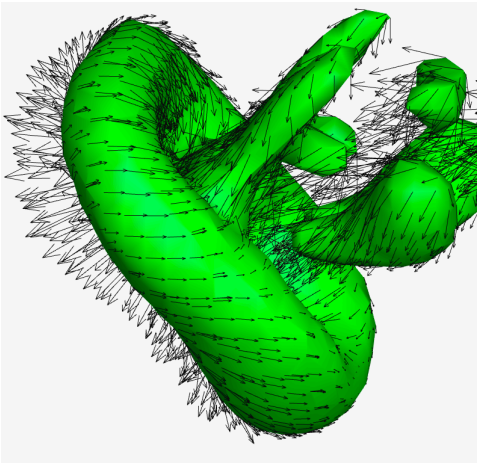

Figure 5. The shape of vortex structures and their surrounding tangential vectors.

4.1.3. Jet Impact

Before the jet impinges on the wall, taking the jet on the left-hand side of the mold as an example, Figure 6a–c demonstrates the transient impact process of the vortex structure in the jet flow at different stages. Before the impact of the jet, the head of the jets presents a "ring-shape" vortex with the rotation vector and connects the "rib-shape" structures in the middle position of the vortex ring. When the jet impinges on the narrow wall, the "ring" vortex appears to increase first, and then decreases due to the influence of the wall. The significant change in the vortex structure occurs and cause strong oscillation. The vortex ring with the braided region can be divided into two smaller vortex rings at the impact point. The "rib-shape" structures in the middle of the vortex ring are also broken, and the "rib-shape" vortices develop together with the vortex ring. It is also found that the tangential vectors around the upper vortex ring (after separation) tend to point upwards. In contrast, the lower vortex shows the downward tangential vector thereof. After the impact of the jet, the upward and downward vortex rings break more complex vortices.

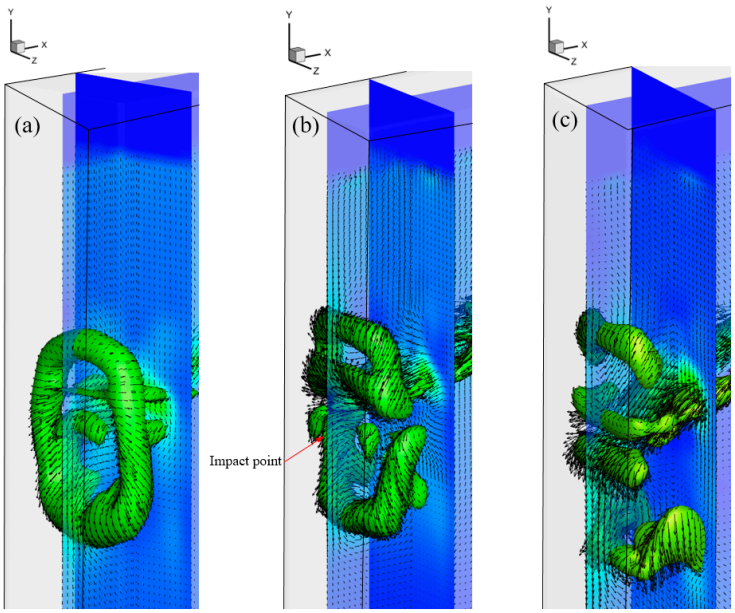

Figure 6. The transient process of the impact of the vortex structure in the jet flow at the narrow wall of the mold at different stages: (**a**) before the impact; (**b**) during the impact; (**c**) after the impact.

To describe the relationship between the ring vortex and its surrounding turbulence, Figure 7 illustrates the effective viscosity of steel along its narrow wall on the center plane

of the mold. The viscosity distributions are described around the jet flow and the vortex structures. At the point of the jet impact nearest to the narrow wall, the viscosity around the vortex at the impact point is more evident. With the impact of the jet and the breaking of the vortex, the viscosity around the separated vortex decreases accordingly. Combined with the analysis of Figure 6, the relationship between the vortex structure and the surrounding viscosity reveals the vortex structure formation and turbulent changes in the jet flow region.

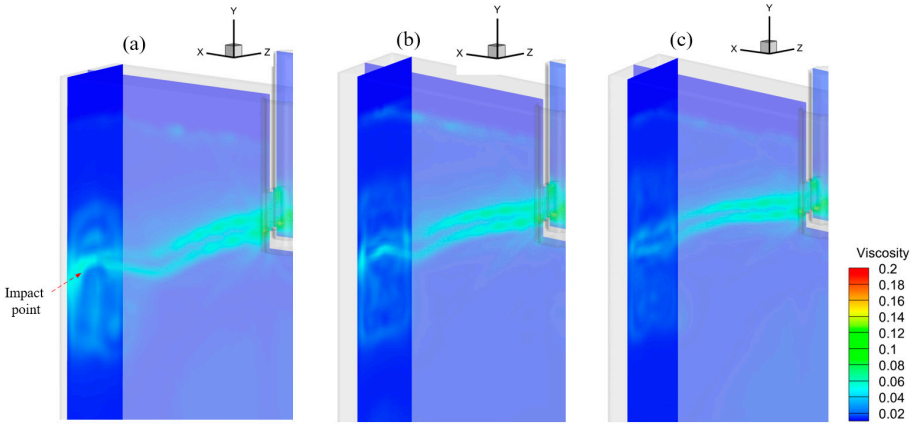

Figure 7. Effective viscosity of steel around the jet flow and the vortex structures along width wall on the center-plane of the mold at different stages: (**a**) before the impact; (**b**) during the impact; (**c**) after the impact.

After the jet impinged on the wall, a turbulent flow formed the two streams in this region: one flows upwards along the free surface, the other moves downwards to greater depth in the mold pool. In this typical flow region near the mold wall, the vortex structures form an asymmetric distribution at the point of impact along the narrow wall of the mold (Figure 8). One part of the coherent vortices is accumulated near the free surface of the mold, and the other spreads from the narrow wall towards a lower position, producing a significant oscillation in the flow within the mold. The results show that the upper and lower patterns of coherent structures at the impact point are asymmetrical near the wall.

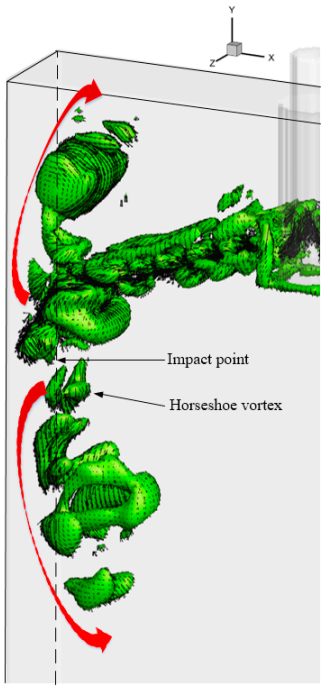

Figure 8. Distribution of coherent structures at impact point along the narrow wall of the mold.

Various types of vortices structures play an essential role in the development of turbulence in the mold. In addition to the "ring" and "rib" -like shaped vortices present in the jets (Figure 6), "horseshoe" vortices are also found in the turbulent flow near the wall of the mold (Figure 8). To further study the formation of the "horseshoe" vortex in the turbulent flow, Figure 9 shows the structure of the "horseshoe" vortex near the narrow wall of the mold. These "horseshoe vortices" consist of the vortex head and its leg. It is noticed that the vortex head with span-wise vorticity develops upward at an angle of about 45 degrees along the wall. In the movement of the "horseshoe" vortex, the ends of two legs near the wall gradually stretch and deform along the flow direction. The fluid between the head and leg forms a strong upward ejection phenomenon, while the fluid at the bottom of the leg sweeps along the wall direction. Thus, the "horseshoe" vortex is temporally unstable and promotes the development of turbulence, which leads to the instability of the flow near the wall of the mold.

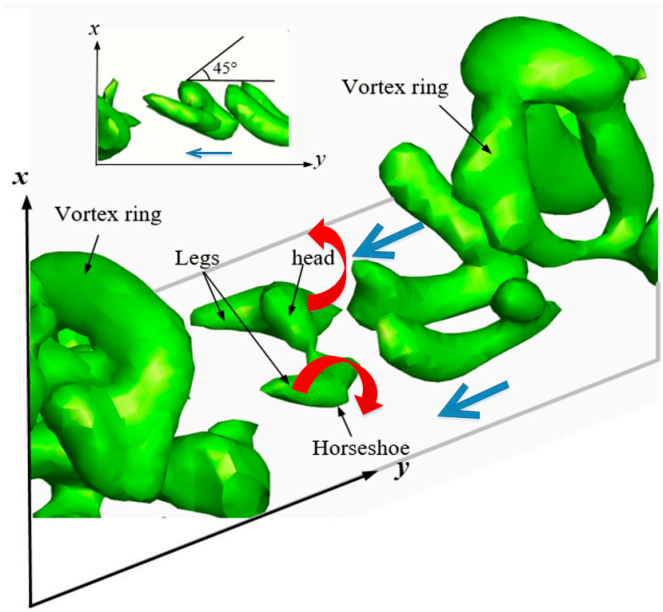

Figure 9. Structures of the "horseshoe" vortex near the narrow wall of the mold.

4.2. Comparison of Different Criteria

Vortex identification is based on the idea of function and field theory. The information of the flow field is then calculated to determine the function, which can describe the vortex by means of the isosurface. The more commonly used vortex identifications with translation invariance include the vortex method, Q method, $\lambda 2$ method (Lambda-2), Δ method (Delta), Ω method (Omega), etc. The specific principles and formulas can be found elsewhere [27]. These methods of identifying structures describing the upper and lower flow patterns near the wall of the mold are described here.

(1) Vorticity method

The vorticity method is the simplest method to describe vortices, but it is difficult to distinguish the vortices caused by rotations from those caused by shearing (in the boundary layer). The structure of the isosurfaces of vorticity magnitude varies with the threshold. Figure 10 displays the typical flow of the upper and lower streams near the wall of the mold formed by the jet impingement using a vorticity w of 10. The vorticity distribution exhibits substantially symmetrical distribution characteristics. However, it is difficult to identify the vortex structure, especially in a typical flow process.

Figure 10. Typical flow of the upper and lower streams near the wall of the mold and corresponding vortex structures using a vorticity w of 10.

(2) Q method

The Q method is the classic method, with a low computational burden, giving accurate results. Generally, an isosurface value with $Q > 0$ is selected as the vortex. Figure 11 shows the vortex structures of the upper and lower streams with the jet flow (velocity isosurface $v = 0.3$ m/s) near the wall of the mold formed by the jet impingement using a Q criterion ($Q = 10$). The vortex structure exhibits asymmetric distribution characteristics, and various vortex structures can be determined in a typical flow process.

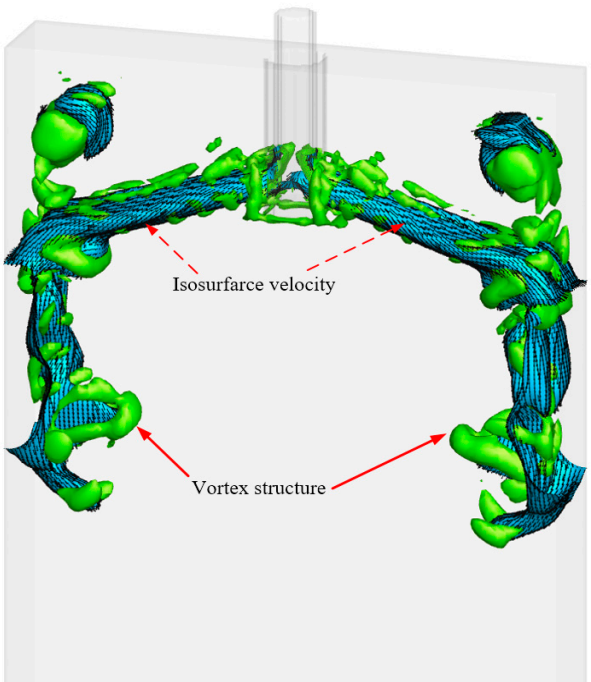

Figure 11. Vortex structures of the upper and lower streams with the jet (velocity isosurface $v = 0.3$ m/s) near the wall of the mold using the Q criterion $Q = 10$.

(3) $\lambda 2$ method

Compared with the Q method, the $\lambda 2$ method is derived from the inviscid and incompressible transport equation using the lowest point of local pressure to determine the position of the vortex. The formula is more complicated. Generally, a specific isosurface value with $\lambda 2 < 0$ is selected as the vortex. Figure 12 shows the vortex structure distribution of the upper and lower streams near the wall of the mold using the Lambda-2 criterion $\lambda 2 = 10$: the vortex structure exhibits asymmetric characteristics.

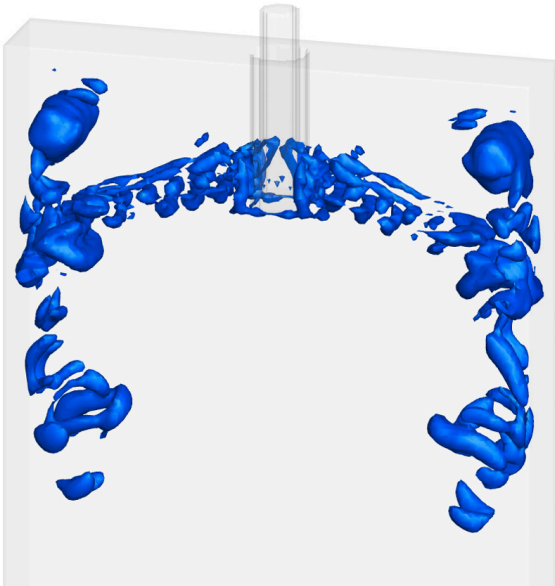

Figure 12. Vortex structures of the upper and lower streams near the wall of the mold formed using the Lambda-2 criterion $\lambda 2 = 10$.

(4) Δ method

A vortex core is a region of space where the vorticity is sufficiently strong to cause the rate-of-strain tensor to be dominated by the rotation tensor, i.e., the velocity gradient tensor has complex eigenvalues. The eigenvalues that are complex can be determined by looking at the sign of the discriminant of the characteristic equation. Generally, the isosurface of any $\Delta > 0$ is selected as the vortex. Figure 13 presents the vortex structures of the upper and lower streams near the wall of the mold formed by the jet impingement using the $\Delta = 200$. The results show that the distributions of vortex structure are akin to those induced by the other methods.

(5) Omega method

The Omega (Ω) method is the latest generation of vortex identification methods with the characteristics of normalized thresholds. The Ω method and the Q method formulae are similar, and the thresholds of the Ω method are normalized on (0, 1), exhibiting both strong and weak eddies. The vortex structure of Ω magnitude varies with the threshold. Figure 14 shows the vortex structures of the upper and lower streams near the wall formed by the jet impingement using the Ω criterion of the thresholds of 0.49, 0.51, 0.53, 0.55, 0.57, and 0.59. By adjusting the Ω thresholds, the method can determine a typical flow structure in the continuous casting mold. The excess region of the vortex structure appears at the bottom of the mold in Figure 14a at $\Omega = 0.49$, which is inconsistent with the typical flow structure selected in the current simulation. Figure 14b–e shows typical vortex structures in the range of different Ω values from 0.51 to 0.57; however, the partial-jet regions at both sides of the SEN are cut off at $\Omega = 0.59$, which are undesired jet flow structures (Figure 14f); therefore, Ω should be selected from the range of 0.51 to 0.57 as an appropriate value of the criterion, which is in agreement with the recommendation $\Omega = 0.52$ [27].

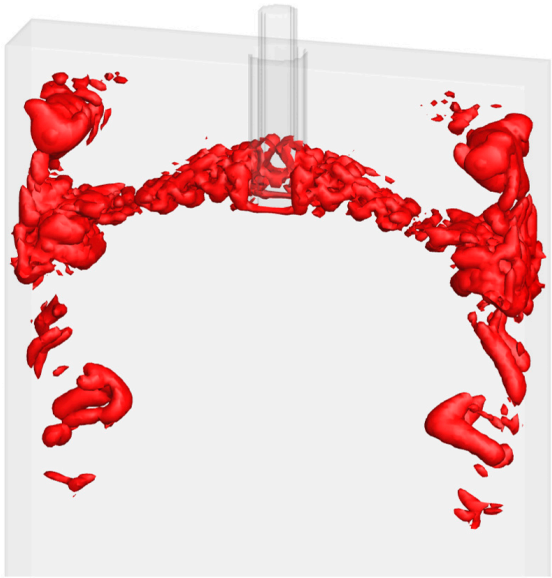

Figure 13. Vortex structures of the upper and lower streams near the wall of the mold formed using the Δ criterion with Δ = 200.

4.3. Periodic Flow

By comparing different methods of vortex structure identification, it is sufficient to obtain the distribution of the vortex structures using the Q criterion in this simulation because other methods are computationally expensive and do not have obvious advantages compared to the Q criterion. In this section, the oscillation flow and the evolution of the vortex structure induced by the Q criterion and corresponding turbulence are studied quantitatively. Figure 15a–c illustrates the evolution of coherent vortices near the narrow wall of the mold when the turbulence is fully developed. The evolution of the coherent vortices is divided into the following stages:

(1) Asymmetric stage: In addition to the asymmetric distribution at the point of impact on the mold wall, coherent vortices are asymmetrically distributed on both sides of the SEN. The vortices structures on the left side of the SEN nozzle are distributed along the wall toward the center of the pool, while those accumulate near the free surface on the right;

(2) Transformation stage: the vortex structures on the left side of the SEN shift to the right, and they are symmetrically distributed on both sides of the SEN within a short period of time;

(3) Mirror stage: The vortex structures of the SEN present a mirror image distribution. The vortex structures on the left side of the SEN move towards the free surface, while those on the right diffused along the sidewall towards the center of the pool at greater depth.

At the time of full development of turbulence, the symmetrical distribution of the circulation at the initial time (Figure 11) becomes asymmetrical (Figure 15), which agrees well with the asymmetric flow seen experimentally. The exchange processes repeat until the next cycle, accompanied by the formation, development, and dissipation of coherent structures. The results of vortex structures show that the asymmetric pattern of coherent structures flows near the wall of the mold exchanges at the upper region on both sides of the SEN, reflecting the periodic flow in the mold.

This phenomenon of flow pattern exchanges in the upper mold may be related to the mechanism of the crossflow between the SEN wall and mold width. For a bifurcated jets flow, Lawson et al. [28,29] also found that this crossflow between SEN wall and mold width is necessary for the presence of self-sustained oscillations in the mold. A schematic illustration of left and right-hand monitoring lines at both sides and Point A in the horizontal crossflow of the SEN is shown in Figure 16. Based on this, the turbulence in

asymmetrical coherent vortices on both sides of the mold and the periodic characteristics via crossflow in the mold are studied.

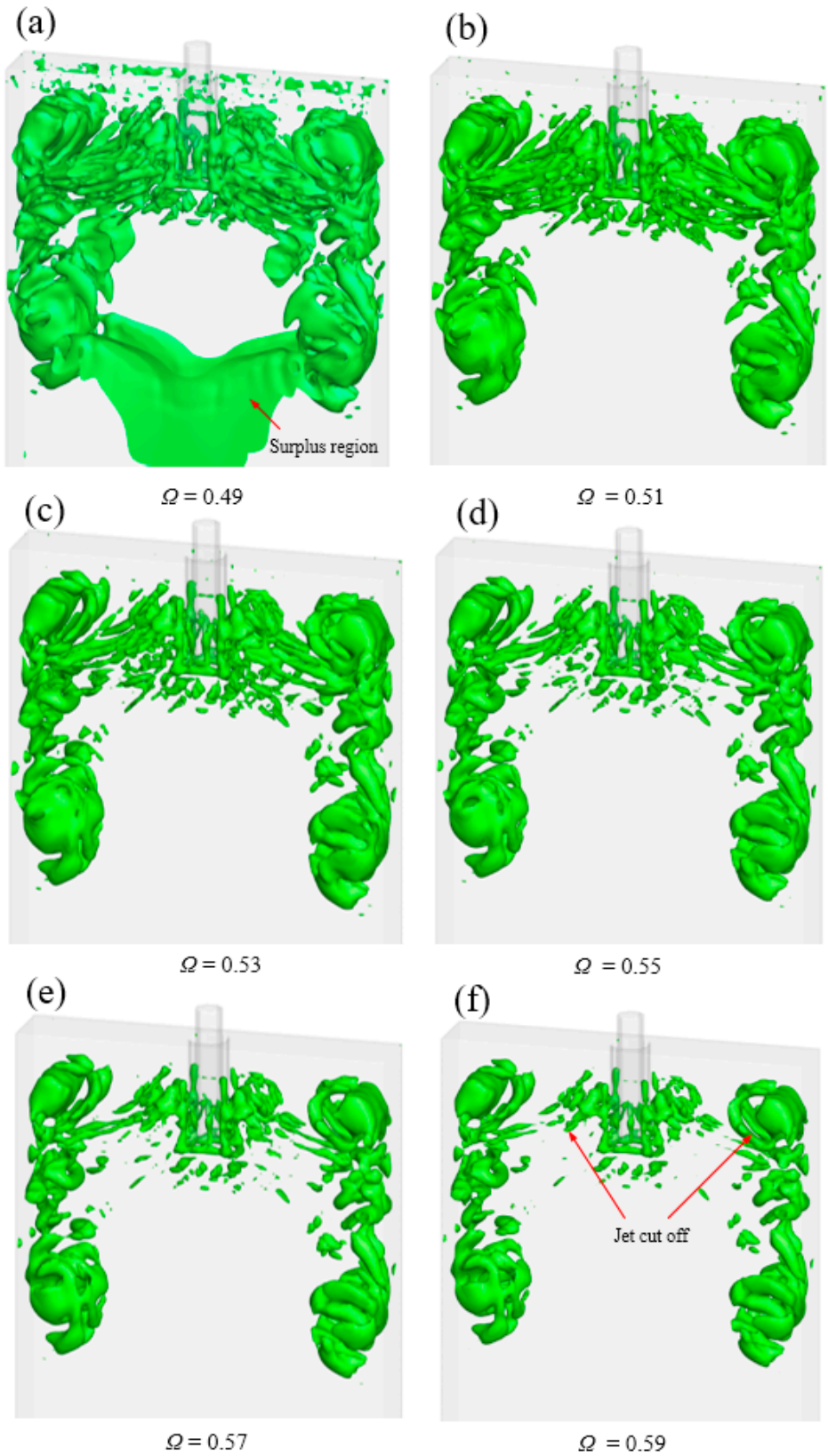

Figure 14. Vortex structures of the upper and lower streams near the wall using the Ω criterion of the thresholds of (**a**) 0.49, (**b**) 0.51, (**c**) 0.53, (**d**) 0.55, (**e**) 0.57, and (**f**) 0.59.

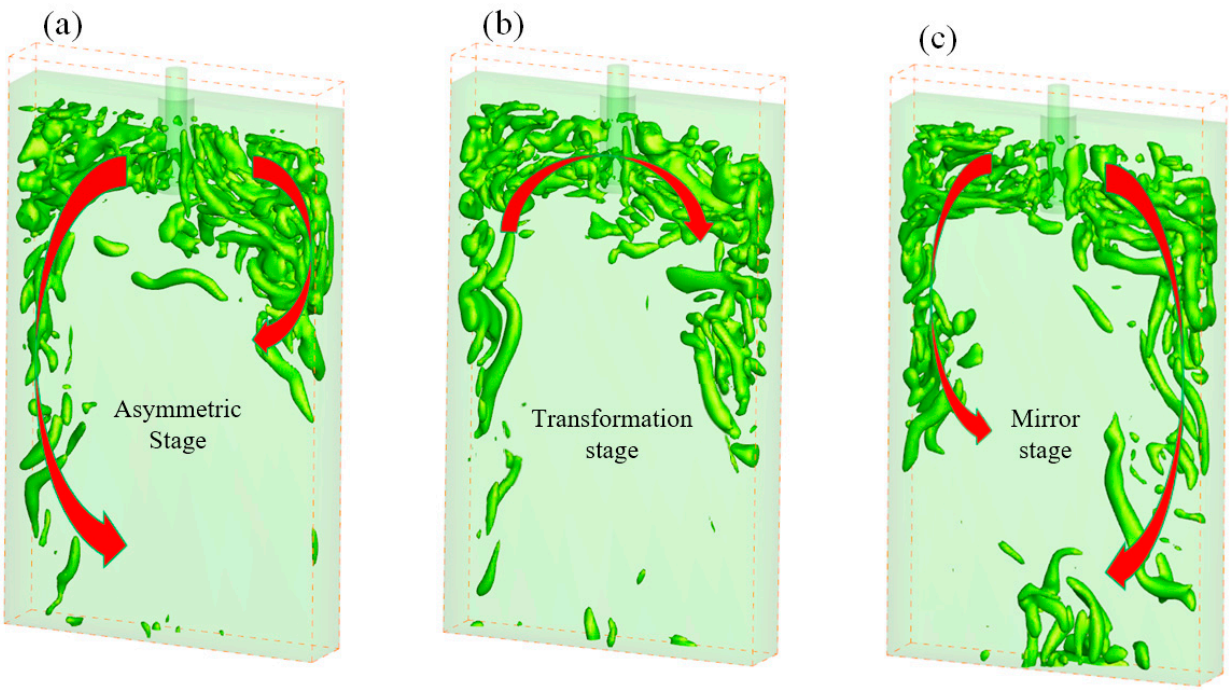

Figure 15. Asymmetric evolution of coherent structures near the narrow wall of the mold at the time of full development of turbulent flow at different stages: (**a**) asymmetry, (**b**) transformation, and (**c**) mirror image.

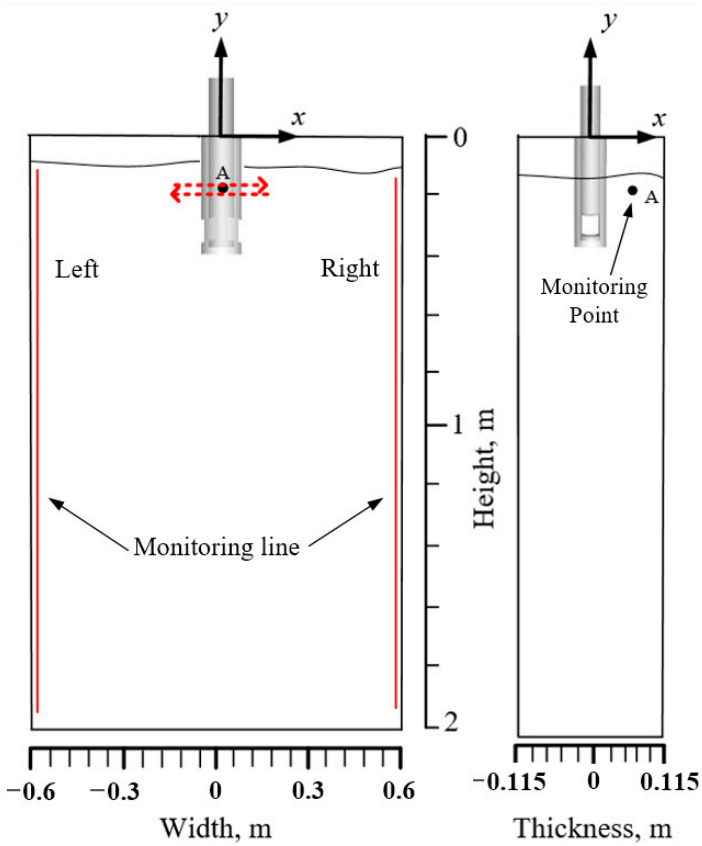

Figure 16. Schematic illustration of the crossflow and the monitoring point A through the gaps between the SEN wall and mold width.

Figures 17–19 show the effective viscosities of the turbulent flow along the centerline at both sides of the mold at corresponding different stages (Figure 15). The turbulent viscosity of flow near the wall of the mold also exhibits asymmetric characteristics. Figure 17 shows the asymmetric viscosity at both sides, where the viscosity on the left is higher than that on the right. Figure 18 shows that the trends of viscosity distribution are consistent on both walls of the mold. Figure 19 demonstrates a mirror image of the viscosity distribution, where the viscosity on the right is higher than that on the left. It is noteworthy that the viscosity first increases, then decreases, and finally increases again at the left or right wall: it can be inferred that the viscosity is related to wobbles in the jet flow upon impact. The turbulent flow (viscosity) can reflect changes in asymmetric vortex structures and flow patterns (via crossflow) inside the mold.

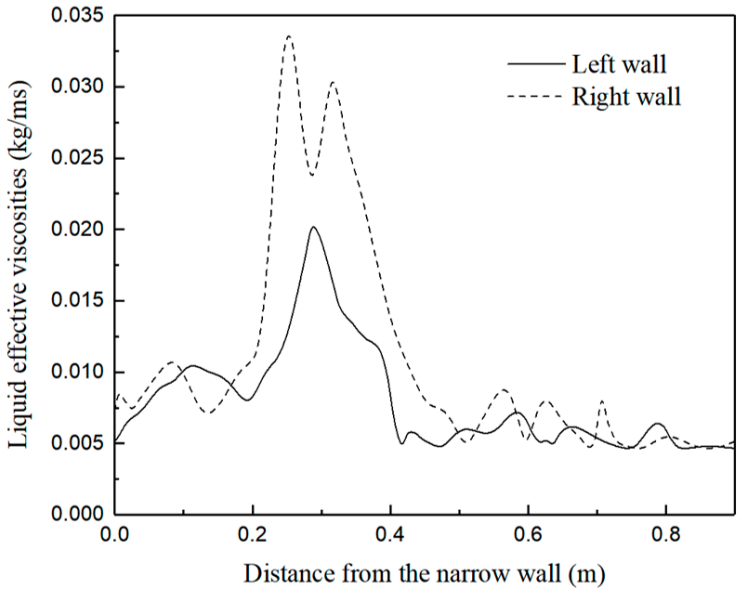

Figure 17. Effective viscosity of the turbulent flow along the centerline at both sides of the mold at the asymmetric stage.

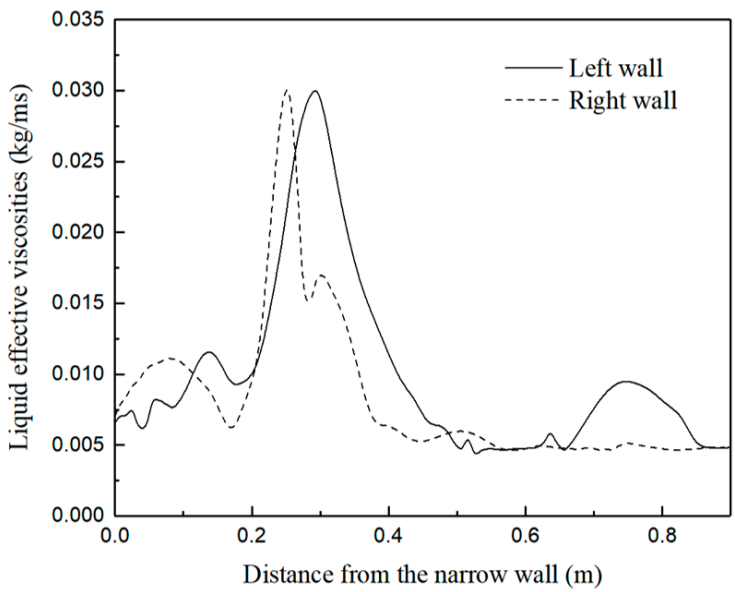

Figure 18. Effective viscosity of the turbulent flow along the centerline at both sides of the mold at the transformation stage.

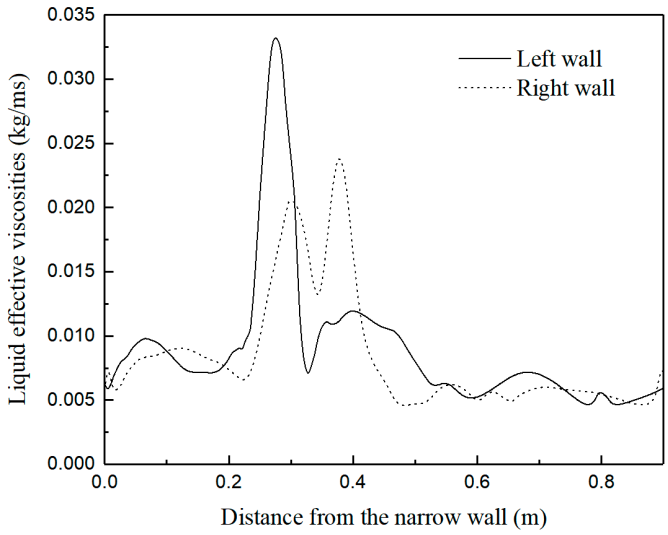

Figure 19. Effective viscosity of the turbulent flow along the centerline at both sides of the mold at the mirror stage.

To quantify the periodic flow and in the mold, the horizontal velocities of the crossflow are analyzed by monitoring at point A via crossflow between the SEN wall and mold width. A fast Fourier transform (FFT) is conducted on the horizontal velocities to obtain a frequency graph representing the effect of each frequency of the spectrum on the amplitude of the signal. The range of amplitude distribution of each frequency in the signal is explained by a finite set of data. In this study, the data are sampled every 0.02 s from the simulation results, and the collected data are 2000 within 30 s. The total time and the sampling interval are kept the same. Figure 20 shows that the frequency of horizontal crossflow is converted by FFT when the casting speed is 1.3 m/min and the SEN immersion depth is 90 mm. Flow oscillation frequencies are mainly concentrated in the range of 0.3 Hz. There are also many different frequencies (0.26 Hz, 0.60 Hz, 0.78 Hz, and 1.28 Hz) observed; it is noted that the peak frequency is 0.26 Hz which represents the flow-oscillation frequency, and the corresponding amplitude exceeds 0.21. The crossflow shows two main components of periodic behavior. The frequency approaching 0.5 Hz is in the low-frequency range. The frequency approaching 1.0 Hz is an intermediate frequency, revealing that the oscillations are not a simple combination of frequency modes of crossflow in the mold.

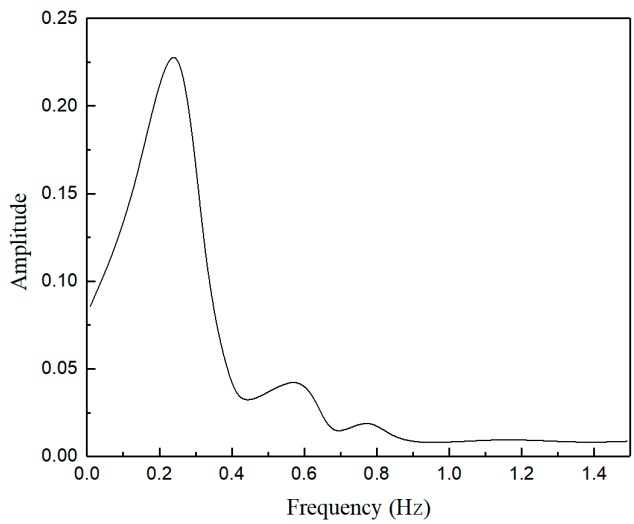

Figure 20. The oscillation frequency of the crossflow at monitoring point A through the gaps between the SEN wall and mold width.

5. Conclusions

An LBM coupled with the LES model is implemented to simulate the transient flow in the mold. From the results, the major conclusions are drawn as follows:

(1) Flow separation occurs at both the upper separation and the lower concave of the SEN, leading to the accumulation of coherent vortices in these regions and intensifying the oscillations of the jet from the SEN outlet. Various vortex structures with different directions are demonstrated during jet impingement, including the ring, rib, and horseshoe-shaped vortices found in the simulation, resulting in complex turbulent flow near the mold wall;

(2) At the initial time, the pattern of coherent structures on both sides of SEN showed a substantially symmetrical distribution, while at the time of full development of the turbulence, the circulations of coherent structures turn into an asymmetrical pattern in the mold. The evolution of the coherent vortices is divided into the following stages: (I) Asymmetric stage: the vortex structures are asymmetrically distributed at the upper and lower point of impact on the mold wall, except for vortex vortices distributed on both sides of the SEN; (II) Transformation stage: the vortex structures on the left side of the SEN shift to the right; (III) Mirror stage: the vortex structures of the SEN present a mirror image distribution;

(3) Different vortex criteria, including the vortex method, Q method, $\lambda 2$ method (Lambda-2), Δ method (Delta), and Ω method (Omega), are compared. The vortex structures derived from these methods are similar. The value of the Ω model is adjusted within the range of 0.51 to 0.57 as an appropriate threshold for the criterion in this study, which is consistent with the recommended value of $\Omega = 0.52$.

(4) The turbulent viscosity of flow near the wall of the mold also exhibits asymmetric characteristics. It can be inferred that the viscosity can reflect changes in asymmetric vortices structures and flow patterns (via crossflow), as reflected in the periodical flow in the mold. Flow oscillation frequencies are mainly concentrated in the range of 0.3 Hz in this simulation. The oscillations are not simple combinations of frequency modes of crossflow inside the mold.

Author Contributions: Software, P.Z.; validation, P.Z.; investigation, P.Z.; writing—original draft preparation, P.Z.; writing—review and editing, R.P.; funding acquisition, P.Z. and R.P. All authors have read and agreed to the published version of the manuscript.

Funding: The authors are grateful to the National Natural Science Foundation of China (Grant No. 51174122, U1960101) and Anhui University of science and technology introduction of talent research start-up fund project (No.13200456).

Institutional Review Board Statement: Not applicable.

Informed Consent Statement: Not applicable.

Data Availability Statement: Not applicable.

Acknowledgments: National Engineering Laboratory for Vacuum Metallurgy, Kunming University of Science and Technology for the financial support; Institute of Metallurgical Multiphase Transport and Reaction Engineering, School of Metallurgy, Northeastern University.

Conflicts of Interest: The authors declare no conflict of interest.

References

1. Lee, P.D.; Ramirez-Lopez, P.E.R.; Mills, K.C.; Santillana, B. The "butterfly effect" in continuous casting. *Ironmak. Steelmak.* **2012**, *39*, 244–253. [CrossRef]
2. Mills, K.C.; Ramirez-Lopez, P.R.; Lee, P.D.; Santillana, B.; Thomas, B.G.; Morales, R. Looking into continuous casting mould. *Ironmak. Steelmak.* **2014**, *41*, 242–249. [CrossRef]
3. Thomas, B.G. Review on modeling and simulation of continuous casting. *Steel Res. Int.* **2018**, *89*, 1700312. [CrossRef]
4. Wu, M.; Vakhrushev, A.; Ludwig, A.; Kharicha, A. Influence of forced convection on solidification and remelting in the developing mushy zone. *IOP Conf. Ser. Mater. Sci. Eng.* **2016**, *117*, 012045. [CrossRef]

5. Cho, S.M.; Liang, M.; Olia, H.; Das, L.; Thomas, B.G. Multiphase flow-related defects in continuous casting of steel slabs. In Proceedings of the TMS 149th Annual Meeting & Exhibition Supplemental Proceedings, San Diego, CA, USA, 23–26 February 2020; Springer: Cham, Switzerland, 2020.
6. Vakhrushev, A.; Kharicha, A.; Karimi-Sibaki, E.; Wu, M.; Ludwig, A.; Nitzl, G.; Tang, Y.; Hackl, G.; Watzinger, J.; Eckert, S. Generation of reverse meniscus flow by applying an electromagnetic brake. *Metall. Mater. Trans. B* **2021**, *52*, 3193–3207. [CrossRef]
7. Kharicha, A.; Vakhrushev, A.; Karimi-Sibaki, E.; Wu, M.; Ludwig, A. Reverse flows and flattening of a submerged jet under the action of a transverse magnetic field. *Phys. Rev. Fluids* **2021**, *6*, 123701. [CrossRef]
8. Thomas, B.G.; Cho, S.M. Overview of electromagnetic forces to control flow during continuous casting of steel. *IOP Conf. Ser. Mater. Sci. Eng.* **2018**, *424*, 012027. [CrossRef]
9. Cho, S.M.; Thomas, B.G. Electromagnetic effects on solidification defect formation in continuous steel casting. *JOM* **2020**, *72*, 3610–3627. [CrossRef]
10. Liu, Z.; Li, B.; Vakhrushev, A.; Wu, M.; Ludwig, A. physical and numerical modeling of exposed slag eye in continuous casting mould using euler-euler approach. *Steel Res. Int.* **2019**, *90*, 1800117. [CrossRef]
11. Real, C.; Miranda, R.; Vilchis, C.; Barron, M.; Hoyos, L.; Gonzalez, J. Transient internal flow characterization of a bifurcated submerged entry nozzle. *ISIJ Int.* **2006**, *46*, 1183–1191. [CrossRef]
12. Yuan, Q.; Vanka, S.P.; Thomas, B.G.; Sivaramakrishnan, S. Computational and experimental study of turbulent flow in a 0.4-scale water model of a continuous steel caster. *Metall. Mater. Trans. B* **2004**, *35*, 967–982. [CrossRef]
13. Wu, Y.; Liu, Z.; Li, B.; Gan, Y. Numerical simulation of multi-size bubbly flow in a continuous casting mould using population balance model. *Powder Technol.* **2022**, *396*, 224–240. [CrossRef]
14. Wu, Y.; Liu, Z.; Wang, F.; Li, B.; Gan, Y. Experimental investigation of trajectories, velocities and size distributions of bubbles in a continuous-casting mould. *Powder Technol.* **2021**, *387*, 325–335. [CrossRef]
15. Liu, Z.; Li, B.; Jiang, M. Transient asymmetric flow and bubble transport inside a slab continuous-casting mould. *Metall. Mater. Trans. B* **2014**, *45*, 675–697. [CrossRef]
16. Li, X.; Li, B.; Liu, Z.; Niu, R.; Liu, Y.; Zhao, C.; Yuan, T. Large eddy simulation of multi-phase flow and slag entrapment in a continuous casting mould. *Metals* **2019**, *9*, 7. [CrossRef]
17. Liu, Z.; Vakhrushev, A.; Wu, M.; Kharicha, A.; Ludwig, A.; Li, B. Scale-Adaptive Simulation of transient two-phase flow in continuous-casting Mould. *Metall. Mater. Trans. B* **2019**, *50*, 543–554. [CrossRef]
18. Zhao, P.; Li, Q.; Kuang, S.B.; Zou, Z. LBM-LES simulation of the transient asymmetric flow and free surface fluctuations under steady operating conditions of slab continuous casting process. *Metall. Mater. Trans. B* **2017**, *48*, 456–470. [CrossRef]
19. Pirker, S.; Kahrimanovic, D.; Schneiderbauer, S. Secondary vortex formation in bifurcated submerged entry nozzles: Numerical simulation of gas bubble entrapment. *Metall. Mater. Trans. B* **2015**, *46*, 953–960. [CrossRef]
20. He, X.; Luo, L.S. Theory of the lattice Boltzmann method: From the Boltzmann equation to the lattice Boltzmann equation. *Phys. Rev. E* **1997**, *56*, 6811. [CrossRef]
21. Bhatnagar, P.L.; Gross, E.P.; Krook, M. A model for collision processes in gases. I. Small amplitude processes in charged and neutral one-component systems. *Phy. Rev.* **1954**, *94*, 511. [CrossRef]
22. Smagorinsky, J. General circulation experiments with the primitive equations: I. The basic experiment. *Weather Rev.* **1963**, *91*, 99–164. [CrossRef]
23. Anderl, D.; Bogner, S.; Rauh, C. Free surface lattice Boltzmann with enhanced bubble model. *Comput. Math. Appl.* **2014**, *67*, 331–339. [CrossRef]
24. Van Driest, E.R. On turbulent flow near a wall. *J. Spacecr. Rockets* **1956**, *23*, 1007–1011. [CrossRef]
25. Thomas, B.G.; Huang, X.; Sussman, R.C. Simulation of argon gas flow effects in a continuous slab caster. *Metall. Mater. Trans. B* **1994**, *25*, 527–547. [CrossRef]
26. Hunt, J.C.R.; Wray, A.A.; Moin, P. Eddies, streams, and convergence zones in turbulent flows. In *Proceedings of the Summer Program*; Center for Turbulence Research: Stanford, CA, USA, 1988; pp. 193–208. Available online: https://ntrs.nasa.gov/api/citations/19890015184/downloads/19890015184.pdf (accessed on 10 January 2022).
27. Holmén, V. Methods for Vortex Identification. Master's Theses, Mathematical Sciences. Lund University, Lund, Sweden, 2012.
28. Lawson, N.J.; Davidson, M.R. Oscillatory flow in a physical model of a thin slab casting mould with a bifurcated submerged entry nozzle. *J. Fluids Eng.* **2002**, *124*, 535–543. [CrossRef]
29. Lawson, N.J.; Davidson, M.R. Crossflow characteristics of an oscillating jet in a thin slab casting mould. *Fluids Eng.* **1999**, *121*, 588. [CrossRef]